Self-assembled multiferroic epitaxial BiFeO3-CoFe2O4 nanocomposite thin films grown by rf magnetron sputtering

Journal:	*Journal of Materials Chemistry C*
Manuscript ID	TC-ART-03-2018-001192.R1
Article Type:	Paper
Date Submitted by the Author:	18-Apr-2018
Complete List of Authors:	Kim, Tae Cheol; Myongji university, Department of materials science and engineering Ojha, Shuchi ; Massachusetts Institute of Technology Tian, Guo; Massachusetts Institute of Technology Lee, Seung Han ; Myongji University - Natural Science Campus Jung, Hyun Kyu; Myongji University - Natural Science Campus Choi, Jun Woo; KIST, Kornblum, Lior; Technion - Israel Institute of Technology, Andrew and Erna Viterbi Dept. of Electrical Engineering Walker, Frederick; Yale University, Center for Research on Interface Structures and Phenomena; Yale University, Department of Applied Physics Ahn, Charles; Yale University, Applied Physics Ross, Caroline; MIT, Kim, Dong Hun; Myongji university, Department of materials science and engineering

Self-assembled multiferroic epitaxial $BiFeO_3$-$CoFe_2O_4$ nanocomposite thin films grown by rf magnetron sputtering

Tae Cheol Kim,[1] Shuchi Ojha,[2] Guo Tian,[2] Seung Han Lee,[1] Hyun Kyu Jung,[1] Jun Woo Choi,[3] Lior Kornblum,[4] Frederick J. Walker,[5] Charles H. Ahn,[5] Caroline A. Ross,[2,*] and Dong Hun Kim[1,*]

[1] Department of Materials Science and Engineering, Myongji University, Yongin, Republic of Korea

[2] Department of Materials Science and Engineering, Massachusetts Institute of Technology, Cambridge, Massachusetts, 02139, USA

[3] Center for Spintronics Research, Korea Institute of Science and Technology, Seoul, Republic of Korea

[4] Andrew & Erna Viterbi Dept. of Electrical Engineering, Technion - Israel Institute of Technology, Haifa, 32000, Israel

[5] Department of Applied Physics, Yale University, New Haven, CT, 06520, USA

*) Author to whom correspondence should be addressed. Electronic mail: dhkim@mju.ac.kr and caross@mit.edu

Abstract

Self-assembled nanocomposites consisting of ferrimagnetic $CoFe_2O_4$ and ferroelectric $BiFeO_3$ were grown on Nb-doped $SrTiO_3$ (001) or SrTiO3-buffered Si (001) substrates using radio frequency magnetron sputtering. The spinel $CoFe_2O_4$ formed as epitaxial pillars within a perovskite BiFeO3 matrix, similar to nanocomposites grown by pulsed laser deposition. $CoFe_2O_4$ and $BiFeO_3$ grew with cube-on-cube epitaxy on Nb-doped $SrTiO_3$, with partial relaxation of the in-plane strain of the $BiFeO_3$. The sputter-grown nanocomposites showed an out-of-plane magnetic easy axis as a result of both the shape anisotropy of the pillars and the magnetoelastic anisotropy of the $CoFe_2O_4$, but the latter was dominant. The $BiFeO_3$ matrix exhibited ferroelectric domains, and removing the $BiFeO_3$ led to reduction of magnetic anisotropy by strain relaxation of the $CoFe_2O_4$. For potential application to devices, nanocomposites were integrated on buffered silicon substrates. Templating of the $CoFe_2O_4$ nanopillars was achieved by substrate patterning. These techniques facilitate incorporation of multiferroic nanocomposites into memory and other devices.

Introduction

Self-assembled nanocomposite thin films, consisting of a ferroelectric phase and a ferromagnetic phase grown epitaxially on a substrate, are of great interest for their multiferroic and magnetoelectric properties. The vertically-aligned nanostructure, which is produced by co-deposition of a magnetic spinel and a ferroelectric perovskite on a perovskite substrate, consists of magnetic pillars embedded in a ferroelectric matrix.[1-3] Strain coupling at the vertical interface between the piezoelectric and magnetostrictive phases plays an important role in determining the magnetic, ferroelectric and magnetoelectric response.[4-6] Among many perovskite-spinel nanocomposites, the combination of magnetostrictive $CoFe_2O_4$ (CFO, magnetostriction constant, $\lambda_{100,\ \mathrm{CFO}}$ = (-250 to -590) × 10^{-6})[7] and piezoelectric $BiFeO_3$ (BFO, piezoelectric coefficient, $d_{33,\ \mathrm{BFO}} \approx 60$ pm V^{-1})[8] has been actively investigated because of its well-defined self-assembled nanostructure and its magnetoelectric behavior which is mediated by strain transfer at the interfaces between the two phases.[9-10] Li *et al.* reported the strain-mediated magnetoelectric coupling in a quasi (0−3) nanocomposite heterostructure.[11] In most reported BFO-CFO nanocomposites grown on (001)-oriented $SrTiO_3$, both phases have a cube-on-cube orientation relationship with the substrate and the CFO forms rectangular pillars bounded by <110> facets.[12-14] The BFO is perovskite-structured but has a pseudo-cubic unit cell due to distortion along a [111] axis, and is therefore described as rhombohedral BFO. These nanocomposites have received considerable attention for potential applications in magnetoelectric memory or logic devices.[3-4, 12-14]

These nanocomposites have been exclusively grown using pulsed laser deposition (PLD). PLD enables the growth of high quality epitaxial thin films from an energetic plume of material which is ejected from a target using a high energy laser. However, the substrate area coated in PLD systems is small, and the application of PLD to make uniform films on the wafer level is challenging.[15-16] In contrast, the growth of nanocomposites by sputtering could provide a path towards large scale and low cost devices. The sputtered film is formed from particles ejected from a solid target material via momentum exchange from bombardment with energetic ions such as Ar^+. Sputtering has been used to grow complex oxides such as perovskites, spinels or garnets[17-19] but there is very little work on sputtered nanocomposites. The growth of $BaTiO_3$-CFO using sputtering has been reported,[20-22] but a clear columnar nanocomposite with a facetted structure was not observed, and the magnetic, ferrolectric, and multiferroic behavior of sputter-grown nanocomposite films remains to be explored.

The formation of nanocomposites is governed by kinetic factors such as the mobility of arriving species on the surface, and therefore the morphology and properties of nanocomposites are expected to depend on the vapor deposition process used. Herein we report on the growth, morphology, and microstructure of self-assembled epitaxial BFO-CFO nanocomposites fabricated using radio frequency (RF) magnetron sputtering, and compare the results with those of PLD films.[23-26] Both rhombohedral and tetragonal BFO phases grow depending on the oxygen flow, and the magnetic anisotropy of the CFO is dominated by the strain state. BFO-CFO nanocomposites were integrated on Si substrates via a $SrTiO_3$ buffer layer grown by molecular beam epitaxy to investigate the possible application of nanocomposites in large scale, low cost devices. Finally, the locations of the CFO pillars were templated by pits formed in the substrate by focused ion beam (FIB) patterning. The growth of templated multiferroic nanocomposites by sputtering and their integration on Si will facilitate the incorporation of these materials into magnetoelectric devices.

Experimental

BFO-CFO nanocomposite thin films were fabricated using RF magnetron sputtering from a composite ceramic target prepared by a conventional oxide sintering method. First, the synthesis of BFO powder from Bi_2O_3 (Samchun, Korea, 99.9 %) and Fe_2O_3 powders (Alfa Aesar, 99.9 %) was optimized as shown in **Figure S1**. The phases that formed varied with synthesis temperature due to the volatility of the Bi. CFO powder was prepared from raw materials consisting of Co_3O_4 (Alfa Aesar, 99.9 %) and Fe_2O_3. The powders were mixed by ball milling for 24 hours then calcined at 1200 ˚C for 3 hours in air. The final composite target was prepared from BFO and CFO powders with BFO:CFO molar ratios of 2:1. The powders were mixed using ball milling for 24 hours then dried and pressed into a pellet and sintered at 800 ˚C for 5h in air. The 2 inch diameter sintered target was polished then bonded to a Cu plate (99.99 %) using indium shot (Alfa Aesar, 99.99%) on a hot plate at 200 ˚C.

BFO-CFO nanocomposite films were grown on (001) oriented 1 wt. % Nb-doped $SrTiO_3$ substrates (Nb:STO, lattice parameter $a_{Nb:STO}$ = 3.905 Å, from MTI Corp.) with resistivity 0.007 - 0.1 ohm·cm to enable characterization of the structure and ferroelectric properties. Deposition was conducted at substrate temperatures of 480 - 650 ˚C and samples were cooled down to room temperature while maintaining the deposition atmosphere. The working pressure was 50 mTorr with Ar:oxygen ratios of 1:4 and 1:9. The chamber was initially pumped to 5×10^{-6} Torr base pressure and the RF power was 60 W. Typical film thicknesses were ~200 nm. The nanocomposites grown at a substrate temperature of 480 ˚C were heat treated in a box furnace in air for 1 hour at 600 ˚C or 650 ˚C with a heating and cooling rate of 5 ˚C /min. Some nanocomposites were etched in 10 % dilute hydrochloric acid (HCl) for 1 - 3 minutes and rinsed in DI water to remove the BFO phase.

To integrate the nanocomposites on Si substrates, an 8 nm thick STO layer was grown on a Si (100) substrate using an MBE process as reported elsewhere.[23] Nanocomposites were also grown on Nb:STO substrates that were patterned using a focused ion beam (FIB) to form a square array of pits.[24] A thin layer of CFO was then deposited using PLD which formed seed crystals within the pits. These served as nucleation sites for the sputtered CFO pillars, leading to the formation of a sputtered nanocomposite film consisting of square-symmetry arrays of CFO pillars within a BFO matrix.

The crystal structure and phase formation of the target and films were characterized by X-ray diffraction (XRD-7000, Shimadzu) with a wavelength of $\lambda = 1.54056$ Å. Strain states, phi scans, and reciprocal space mapping (RSM) for in-plane and out-of-plane lattice parameters of the nanocomposites were measured using high resolution XRD (HRXRD, Bruker-AxsD8). Surface morphology was imaged with scanning electron microscopy (SEM, HITACHI, S-4800). Composition analysis of the composite target was carried out using energy dispersive spectroscopy (EDS) in the SEM. The vertically-aligned CFO pillars in BFO matrix were investigated using high resolution transmission electron microscopy (HRTEM, JEM-2100F) operated at 200 kV. Cross-sectional TEM samples were prepared by FIB after depositing a Pt layer in an ion beam coater and Pt/carbon layers in the FIB. A TEM sample was cut with its plane normal to the Nb:STO [110] axis, so the TEM zone axis is [110] for both the BFO and CFO. The magnetic hysteresis loops were measured by vibrating sample magnetometer (VSM, ADE model 1660) at room temperature. Magnetic field was applied from -15 kOe to 15 kOe along the in-plane and out-of-plane directions. Magnetization was reported as the net moment per total volume of the films instead of being normalized to the volume of the magnetic spinel phase. The linear background signal from the substrate, double-sided tape, and quartz holder was subtracted. The ferroelectric properties were measured by piezoresponse force microscopy (PFM) with a scanning probe mode (Cypher, Asylum Research) using conductive PFM probes (Nanoworld).

Results and Discussion

A nanocomposite film grown at 480 ˚C at a pressure of 50 mTorr with Ar:O_2 ratio of 1:4 and RF power of 60 W showed no perovskite or spinel peaks in XRD and had a smooth surface indicative of a non-crystalline film. Annealing at 600 ˚C produced a few facetted features, whereas annealing at 650 ˚C led to a larger number of oriented crystals visible at the film surface. The annealed film contained both CFO and BFO with near-bulk lattice parameters ($a_{\text{bulk, BFO}} = 3.965$ Å[27], $a_{\text{bulk, CFO}} = 8.392$ Å (JCPDS # 22–1086)), and the microstructure is believed to consist of nanocrystals of CFO within a BFO matrix, rather than a columnar structure. The morphology and magnetic properties of the annealed films are described in the supplementary information, **Figure S2**.

The deposition temperature was increased to obtain a columnar nanocomposite. A BFO-CFO film was sputtered on a Nb:STO substrate at 650 ˚C at a pressure of 50 mTorr with Ar:O_2 ratio of 1:4 and RF power of 60 W. The plan-view morphology (**Figure 1 (a)**) shows rectangular CFO pillars with edge lengths of 30 - 50 nm oriented along the <110> directions of the substrate, embedded within the BFO. The [001] and [010] directions of the substrate are drawn in the figure, and are consistent for all SEM top view images in this article. The BFO matrix formed a terraced surface morphology with steps along <100>. The structure resembles that of PLD-grown nanocomposites on STO substrates,[3-4, 8-14] which are typically deposited at a substrate temperature of around 650 ˚C to produce self-assembled CFO pillars in a BFO matrix.

The nanocomposite showed only (00*l*) peaks of CFO and BFO, **Figure 1 (b)**. The out-of-plane lattice parameters were c_{BFO} = 3.985 ± 0.002 Å and c_{CFO} = 8.340 ± 0.004 Å. Unlike the bulk-like unit cell parameter of the sample formed by annealing (**Figure S2**), the BFO exhibits an out-of-plane tensile strain and the CFO exhibits compressive strain as a result of epitaxy at the vertical interfaces. φ scans show that both phases grew epitaxially on Nb:STO substrate with four-fold symmetry (**Figure 1 (c))**. The 2θ angles for Nb:STO (202), BFO (202), and CFO (404) were 67.94˚, 66.76˚, and 62.66˚, respectively and the tilting angle was 45.5˚. The φ-scans confirmed the cube-on-cube epitaxial growth of BFO and CFO on Nb:STO with the relationship of [100] BFO (001) || [100] Nb:STO (001) and [100] CFO (001) || [100] Nb:STO (001) (referred to the pseudocubic BFO lattice), shown in the inset in **Figure 1 (d)**.

Figure 1 (d) presents the RSM of the BFO-CFO nanocomposite around the asymmetric Nb:STO (013) peak. The Nb:STO peak yielded 3.905 ± 0.002 Å for both the in-plane and out-of-plane lattice parameters which matches that of bulk STO. The in-plane and out-of-plane lattice parameters of the BFO correspond to a_{BFO} = 3.950 ± 0.010 Å and c_{BFO} = 3.980 ± 0.010 Å (in agreement with the value from **Figure 1 (b)**), i.e. the BFO phase is rhombohedral (R-BFO), with a tetragonal distortion such that c_{BFO}/a_{BFO} = 1.008. The value of a_{BFO} exceeds that of the substrate indicating partial strain relaxation. The unit cell volume of BFO was 62.098 $Å^3$ which is comparable with that of bulk R-BFO (62.335 $Å^3$). A CFO peak was not observed and it is assumed that the intensity is too low to give a clear peak.

Figure 2 (a) is a cross-sectional TEM image of the BFO-CFO nanocomposite illustrating the arrangement of the perovskite and spinel phases. The pillars appear brighter and protrude ~ 20 - 30 nm above the BFO. The variations in BFO height are consistent with the terraced top view images shown in

Fig. 2 (a). From **Figure 2 (b)**, the tilted {111} facets at the top of a CFO pillar form an angle of 55˚ with the surface of the substrate. Because the sample was cut along the diagonal direction of the substrate, the zone axis orientation was [110], and the (*lll*) and (*l*00) planes meet at an angle of 55˚.

The left image in **Figure 2 (c)** is a high resolution TEM image showing the interface between BFO and CFO observed along the [110] axis of the substrate. The low magnification TEM image and composition map confirmed that the region on the left is CFO and on the right is BFO. In the CFO pillar two planes corresponding to ($\bar{2}$22) and (004), whose interplanar spacing is 2.43 Å and 2.08 Å respectively, make an angle of 55˚ to the (111) facet at the surface shown in **Figure 2 (b)**. In the BFO matrix, two planes with interplanar spacing of 1.40 Å and 1.99 Å exhibit a perpendicular alignment corresponding to ($\bar{2}$20) and (002) planes. Fast Fourier Transform (FFT) patterns of selected areas are shown on panels on the right, which give diffraction patterns consistent with BFO and CFO along the [110] direction. The FFT image of the entire image area illustrates the epitaxial relationship: [100] R-BFO // [100] CFO on Nb:STO substrate in agreement with the XRD data. Elemental mapping (**Figure 2 (d)**) supports the phase separation of CFO pillars and BFO matrix, showing first the Z-contrast image where heavier elements (Bi) are represented with brighter contrast. The elemental maps show no detectable diffusion of Bi into the pillars nor of Co into the matrix.

The magnetic hysteresis loops measured at room temperature for the nanocomposite grown at 650 ˚C are shown in **Figure 3 (a).** The out-of-plane direction was the easy axis, exhibiting an open loop with saturation magnetization M_s = 70 ± 2 emu/cm^3, remanent magnetization M_r = 45 ± 2 emu/cm^3 and coercive field H_c = 4000 ± 50 Oe. The in-plane direction was a hard axis showing almost zero remanent magnetization. The loop did not saturate at a magnetic field of 15 kOe, and the coercive field was 500 ± 50 Oe. The magnetic anisotropy is attributed to a combination of both the shape and magnetoelastic anisotropies, and the latter is dominant for PLD-grown nanocomposites in which CFO is under out-of-plane compressive strain.[6, 20-21,23]

The shape anisotropy field H_{sh} is given by $4\pi\cdot(N_x - N_z)\cdot M_s$ where N_x and N_z are demagnetizing factors along in-plane and out-of-plane directions. Taking M_s = 400 emu/cm^3 for CFO[26] and assuming rod-shaped pillars with 200 nm height and 40 nm diameter yields H_{sh} = 2.2 kOe. On the other hand, estimating the magnetoelastic anisotropy $H_{me} = \frac{3\lambda_{001} Y \,\varepsilon_{001}}{M_s}$, where λ_{001} is the magnetostriction coefficient (-350×10^{-6}),[9] Y is Young's modulus (141.6 GPa), and ε_{001} is the vertical compressive strain (-0.0062), yields $H_{me} = 23.0$ kOe. Therefore, we conclude that the out-of-plane easy axis is attributed primarily to magnetoelastic anisotropy with a smaller contribution from shape anisotropy. Magnetocrystalline anisotropy does not contribute for the [100]-oriented pillars.

The ferroelectric properties of the BFO in the nanocomposite were confirmed by PFM measurements. A topographic image of BFO-CFO nanocomposite films in a 0.5 x 0.5 μm^2 scan area is shown in **Figure 3 (c)** exhibiting rectangular BFO mesas with ~200 nm side lengths along <100> and smaller rectangular CFO pillars with <110> vertical sides. **Figure 3 (d)** shows the PFM amplitude image with bright contrast corresponding to the piezoresponse of BFO, while no response was detected for the CFO pillars. The polarization of R-BFO ferroelectric domains lies along the <111> pseudocubic directions leading to an out-of-plane component for all domains. A hysteretic phase and a typical butterfly-shape amplitude as a function of bias voltage at a fixed location in the BFO confirmed the ferroelectric polarization, **Figure 3 (b).**

With a change in the Ar:O_2 ratio to 1:9 (but other sputtering conditions the same as for the sample of **Figure 1(a)**), a minority phase of tetragonal structured BFO (T-BFO) appeared together with the majority R-BFO as shown in **Figure 4.** The growth rate was about half that found for an Ar:O_2 ratio of 1:4 and the sputter time was increased to produce the same film thickness. The metastable T-BFO phase has been reported in highly strained nanocomposites grown by PLD on $LaAlO_3$ (001) which imposed a more compressive in-plane strain compared to STO (001) substrates, [28-29] and in nanocomposites grown at low temperature where β-Bi_2O_3 played a seed role. [3, 29] **Figure 4 (a)** shows the plan-view SEM image of the BFO-CFO nanocomposite, in which the shape and orientation of the CFO pillars was the same as for the sample of **Figure 1 (a)**, though with a smaller edge length of ~ 20 nm. The BFO matrix showed a flat morphology attributed to the lower growth rate at the higher oxygen fraction. If the pressure was lowered to 10-30 mTorr at constant RF power of 60 W, the growth rate was higher and the surface was rougher.

XRD showed the T-BFO peaks around 19.0˚ 2θ for the (001) reflection and 38.5˚ for (002), **Figure 4 (b),** yielding an out-of-plane lattice parameter of 4.667 ± 0.003 Å. The higher intensity R-BFO peak was split into two peaks with lattice parameters of 3.968 ± 0.004 Å (similar to the bulk lattice parameter of BFO) and 4.077 ± 0.002 Å. For the CFO, the out-of-plane lattice parameter was 8.338 ± 0.004 Å, similar to that of CFO grown at the lower oxygen ratio. The CFO is under out-of-plane compressive strain in the nanocomposite with mixed phase BFO, just as in nanocomposites with only R-BFO.

The magnetic hysteresis loops of the nanocomposite grown at higher oxygen ratio, **Figure 4 (c),** exhibited an out-of-plane easy axis attributed to the magnetoelastic anisotropy. The saturation magnetization was 68 ± 2 emu/cm^3, while the remanent magnetization were 45 ± 2 and 5 ± 2 emu/cm^3 and coercive fields were 3000 ± 50 Oe and 300 ± 50 Oe for out-of-plane and in-plane loops, respectively. Except for a reduced coercivity, the loops are similar to those in **Figure 3 (a)** suggesting that the mixed phase BFO phase does not play a significantly different role from that of R-BFO in determining the magnetic properties of the CFO. Considering the ferroelectric properties, the nanocomposite with mixed phase BFO showed similar amplitude and a slightly lower coercive electric field compared with those of the nanocomposite with only R-BFO (**Figure 4 (d)** and **Figure 3(b)**). **Figure S3** shows PFM images of the nanocomposite with mixed phase BFO, in which uniformly polarized regions were written using a voltage of ±14 V.

To reveal the effect of the strain at the vertical interfaces on the magnetic properties of the CFO pillars, the mixed-phase BFO sample of **Figure 4** was etched in HCl for 1 min to remove the BFO and reveal free-standing CFO pillars shown in **Figure 5 (a)** and **(b)**. Longer etching times led to toppled or missing pillars, **Figure 5 (c)**. Strain relaxation of CFO as a result of removing the BFO was confirmed from a shift in the CFO x-ray peak position and the disappearance of the BFO peak. **Figure 5 (d)** illustrates the XRD data of unetched, 1 min etched and 3 min etched nanocomposites around the (001), (002), and (003) peaks of Nb:STO. After etching for 1 min the (001), (002), and (003) of relaxed R-BFO and (001), (002) of T-BFO disappeared but the (001), (002), and (003) of strained R-BFO were still present, showing that it was the last part of the BFO to be removed. Its out-of-lattice parameter was 4.078 ± 0.002 Å which is close to that of the unetched sample. After 3 min etching, the only remaining BFO peak was the (002) peak of the strained R-BFO, which had an out-of-plane lattice parameter of 4.040 ± 0.002 Å implying a small amount of strain relaxation compared to the unetched film. Prior works[3, 23-24, 26, 30] have shown that removal of the BFO leads to an increase in the out-of-plane lattice parameter of the CFO due to relaxation of the compressive strain imposed by lattice match with the BFO at the vertical interfaces. Here, the out-of-plane lattice parameter increased from 8.338 ± 0.004 Å for the unetched sample to 8.378 ± 0.002 Å and 8.387 ± 0.002 for 1 and 3 min etched samples, close to the bulk lattice parameter for CFO.

Figure 5 (e) and **(f)** shows the room temperature magnetic hysteresis loops of BFO-CFO nanocomposites after 1 and 3 min etching, which can be compared to the unetched sample, **Figure 4 (c)**. The out-of-plane anisotropy decreased dramatically on etching due to the strain relaxation, as evidenced by the reduction of the hard-axis saturation field from ~9 kOe after 1 min etching to ~5 kOe for 3 min etching, determined from the in-plane loops. The saturation magnetization decreased to 59 ± 2 and 30 ± 2 emu/cm^3 (normalized to the unetched sample volume) for 1 and 3 min etched nanocomposites, attributed to the missing CFO pillars evident in **Figure 5 (c)**. The out-of-plane compressive strain of -0.0017 and -0.0006 for 1 and 3 min etched samples gives a calculated magnetoelastic anisotropy field of 6.2 kOe and 2.2 kOe respectively, which explains the decrease in net anisotropy upon etching. The shape anisotropy field was assumed to be unchanged at 2.2 kOe.

BFO-CFO nanocomposites were grown on STO-buffered (001) Si substrates. The STO buffer grows with a 45° rotated cube-on-cube epitaxy on Si because $\frac{1}{\sqrt{2}}a_{bulk,\ Si}$ = 3.840 Å is close to $a_{bulk,\ STO}$ = 3.905 Å. Nanocomposites were grown at a pressure of 50 mTorr with an Ar:O_2 ratio of 1:4 and RF power of 60 W. The nanocomposites on STO-buffered Si exhibit rectangular CFO pillars with side length of 20-50 nm as shown in **Figure 6 (a)**, similar to that of nanocomposites grown on (001) oriented STO or Nb:STO substrates. The two orthogonal cleavage directions of the Si substrate correspond to [110] and [$\bar{1}$10] of Si and [100] and [010] of STO, BFO and CFO.

Figure 6 (b) depicts the XRD scan of BFO-CFO/STO/Si with (00*l*) STO, R-BFO, T-BFO, CFO, and Si peaks visible. The nanocomposite films contained mixed-phase BFO, unlike the films on Nb:STO substrate which contained only R-BFO phase when grown under the same conditions. The difference may be related to the lower in-plane lattice parameter of the STO buffer layer compared to bulk, to a different temperature of the Si substrate due to its different thermal emissivity compared to Nb:STO, or to a change in sputter conditions because the films were grown several months apart.

The epitaxial STO layer grown by MBE has an out-of-lattice parameter of 3.927 ± 0.003 Å which exceeds that of bulk STO, likely due to non-ideal cation stoichiometry.[31-32] The R-BFO and T-BFO phases were under tensile strain along the out-of-plane direction, attributed to the lattice mismatch with the STO/Si. The out-of-plane lattice parameters of R-BFO and T-BFO were 4.001±0.002, and 4.628±0.004 Å, respectively, exceeding the values for nanocomposites on single crystal STO.

The CFO pillars are under out-of-plane compression with lattice parameter 8.307±0.005 Å, a larger strain than exists in nanocomposites on single crystal STO. This leads to a higher magnetic anisotropy for the nanocomposites on Si, **Figure 6 (c)**, which could not be saturated in fields of 15 kOe. There was also a small low-field kink in the out-of-plane loop suggesting part of the CFO had a different strain state or composition. The estimated magnetoelastic anisotropy field is 37.2 kOe based on the out-of-plane compressive strain of -0.010. We similarly reported an increase in anisotropy for PLD-grown nanocomposites on STO-buffered Si compared with those on STO.[23]

Finally, we demonstrate that the CFO nanopillars can be regularly ordered in the BFO matrix via selective nucleation at designated sites, as illustrated in **Figure 6 (d)**. The templating process was developed for nanocomposites grown by PLD[10, 24, 33]. A FIB-patterned substrate was prepared consisting of pits in a square array with period 67 nm, and CFO nuclei were formed by growing a thin CFO layer by PLD, **Figure 6 (e).** All the pits were occupied by CFO nuclei and a few CFO nuclei were also observed in the regions between the pits. The BFO-CFO nanocomposite was then sputtered at a pressure of 50 mTorr with Ar:O_2 ratio of 1:4 and RF power of 60 W. **Figure 6 (f)** reveals an ordered array of spinel pillars in a perovskite matrix.

These experiments have established a robust growth method for self-assembled oxide nanocomposites within a wide process window of sputter parameters. For example, we have observed self-assembled pillar morphologies for sputter powers in the range of 40 – 80 W, for total pressures of 10 – 50 mTorr and for Ar:O_2 ratios of 1:0 (pure Ar), 1:2, 1:4 and 1:9. Formation of the as-grown columnar microstructure rather than nanocrystals of CFO in a BFO matrix required an elevated substrate temperature of around 650˚C. The sputtered nanocomposites exhibit many similarities to nanocomposites made by PLD. Although there are considerable differences between the two growth processes, both are characterized by energetic species present in the sputter plasma or the PLD plume whose bombardment enhances surface diffusion[34-35] and is assumed to promote the columnar growth structure. Nanocomposites made by PLD and sputtering exhibit the same pillar shape, orientation and even periodicity, and each of the two processes can produce nanocomposites on STO-buffered Si and ordered arrays on a patterned Nb:STO substrate. In both PLD and sputtered films the net magnetic anisotropy of the CFO pillars is dominated by magnetoelastic anisotropy due to epitaxial strain at the vertical interfaces. One notable difference, however, is the formation of mixed phase T-BFO and R-BFO in the nanocomposite under certain sputtering conditions, which has not been observed in PLD nanocomposites on STO.

Conclusions

Self-assembled multiferroic perovskite-spinel BFO-CFO vertical nanocomposites were successfully grown using sputtering, both on single crystal STO substrates and on STO-buffered Si. Deposition at 650˚C yielded a columnar epitaxial structure in which the BFO and CFO grew with a cube-on-cube epitaxy with [100] BFO (001) || [100] Nb:STO (001) and [100] CFO (001) || [100] Nb:STO (001). The nanocomposites exhibited an out-of-plane magnetic easy axis as a result of both shape and magnetoelastic anisotropy. The anisotropy fields increased with the out-of-plane compressive strain in the CFO, and removal of the BFO matrix relaxed the strain and lowered the anisotropy. Ferroelectric switching of the BFO matrix was observed. With a change in Ar:O_2 ratio, a mixed phase T-BFO and R-BFO formed, but the magnetic and ferroelectric properties of the nanocomposite were not significantly changed. Nanocomposites were integrated on Si substrates via a MBE-grown STO buffer layer, and showed similar structure and higher magnetic anisotropy compared to nanocomposites on single crystal STO and Nb:STO substrates. Finally, CFO nanopillars were templated using FIB. This work demonstrates that highly ordered spinel-perovskite nanocomposites can be grown using sputtering on Si substrates which considerably simplifies their integration into devices that take advantage of their multiferroic properties, such as multiferroic memory devices based on magnetic nanopillars in a ferroelectric template.[36]

Author contributions

D.H.K and C.A.R designed the research. T.C.K, S.H.L, and H.K.J grew epitaxial spinel-perovskite nanocomposite thin films. S.O, G.T, and J.W.C performed PFM, HRXRD, and VSM measurements. L.K, F.J.W, and C.H.A prepared high quality epitaxial STO films on Si substrates. All contributed to data discussion and to writing the manuscript.

Conflicts of interest

There are no conflicts to declare.

Acknowledgments

This work was supported by Basic Science Research Program through the National Research Foundation of Korea (NRF) funded by the Ministry of Science, ICT & Future Planning (NRF-2015R1C1A1A01051656) and the KIST Institutional Program. CAR and SO acknowledge the support of FAME, a STARnet Center of MARCO and DARPA. Work at Yale was supported by the NSF under grants DM-1309868 and MRSEC DMR-1119826 (CRISP).

References

1. H. Zheng, J. Wang, S. E. Lofland, Z. Ma, L. Mohaddes-Ardabili, T. Zhao, L. Salamanca-Riba, S. R. Shinda, S. B. Ogale, F. Bai, D. Viehland, Y. Jia, D. G. Schlom, M. Wuttig, A. Roytburd, R. Ramesh, *Science*, 2004, **303**, 661.
2. J. L. MacManus-Driscoll, *Adv. Funct. Mater.*, 2010, **20**, 2035.
3. D. H. Kim, N. M. Aimon, X. Y. Sun, C. A. Ross, *Adv. Funct. Mater.*, 2014, **24**, 2334.
4. W. Zhang, J. Jian, A. Chan, L. Jiao, F. Khatkhatay, L. Li, F. Chu, Q. Jia, J. L. MacManus-Driscoll, H. Wang, *Appl. Phys. Lett.*, 2014, **104**, 062402.
5. H. Wu, G. Chai, T. Zhou, Z. Zhang, T. Kitamura, H. Zhou, *J. Appl. Phys.*, 2014, **115**, 114105.
6. Y. Chen, S. Ojha, N. Tsvetkov, D. H. Kim, B. Yildiz, C. A. Ross, *Cryst. Eng. Comm.*, 2016, **18**, 7745.
7. R. M. Bozorth, E. F. Tilden, A. J. Williams, *Phys. Rev.*, 1955, **99**, 1788.
8. J. Wang, J. B. Neaton, H. Zheng, V. Nagarajan, S. B. Ogale, B. Liu, D. Viehland, V. Vaithyanthan, D. G. Scholm, U. V. Waghmare, N. A. Spaldin, K. M. Rabe, M. Wuttig, R. Ramesh, *Science*, 2003, **299**, 1719.
9. F. Zavaliche, T. Zhao, H. Zheng, F. Straub, M. P. Cruz, P.-L. Yang, D. Hao, R. Ramesh, *Nano Lett.*, 2007, **7**, 1586.
10. N. M. Aimon, D. H. Kim, X. Y. Sun, C. A. Ross, *ACS Appl. Mater. Interfaces*, 2015, **7**, 2263.
11. Y. Li, Z. Wang, J. Yao, T. Yang, Z. Wang, J.-M. Hu, C. Chen, R. Sun, Z. Tian, J. Li, L.-Q. Chen, D. Viehland, *Nat. Commun.*, 2014, **6**, 6680.
12. S.-C. Liao, P.-Y. Tsai, C.-W. Liang, H.-J. Liu, J.-C. Yang, S.-J. Lin, C.-H. Lai, Y.-H. Chu, *ACS Nano.*, 2011, **5**, 4118.
13. H. Zheng, F. Straub, Q. Zhan, P.-L. Yang, W.-K. Hsieh, F. Zavaliche, Y.-H. Chu, U. Dahmen, R. Ramesh, *Adv. Mater.*, 2006, **18**, 2747.
14. A. Chen, Z. Bi, Q. Jia, J. L. MacManus-Driscoll, H. Wang, *Acta Mater.*, 2013, **61**, 2783.
15. R. E. Muenchausen, K. M. Hubbard, S. Foltyn, R. C. Estler, N. S. Nogar, C. Jenkins, *Appl. Phys. Lett.*, 1990, **56**, 578.
16. P. R. Willmott, J. R. Huber, *Rev. Mod. Phys.*, 2000, **72**, 315.
17. H. Adachi, T. Mitsuyu, O. Yamazaki, K. Wasa, *J. Appl. Phys.*, 1986, **60**, 736.
18. Y. Suzuki, *Annu. Rev. Mater. Res.*, 2001, **31**, 265.
19. T. Yoshimoto, T. Goto, R. Isogai, Y. Nakamura, H. Takagi, C. A. Ross, M. Inoue, *Opt. Express*, 2016, **24**, 259974.
20. N. Dix, V. Skumryev, V. Laukhin, L. Fabrega, F. Sanchez, J. Fontcuberta, *Mater. Sci. Eng., B*, 2007, **144**, 127.

21. I. Fina, N. Dix, V. Laukhin, L. Fabrega, F. Sanchez, J. Fontcuberta, *J. Magn. Magn. Mater.*, 2009, **321**, 1795.
22. Q. Yang, W. Zhang, M. Yuan, L. Kang, J. Feng, W. Pan, J. Ouyang, *Sci. Technol. Adv. Mater.*, 2014, **15**, 025003.
23. D. H. Kim, N. M. Aimon, X. Y. Sun, L. Kornblum, F. J. Walker, C. H. Ahn, C. A. Ross, *Adv. Funct. Mater.*, 2014, **24**, 5889.
24. N. M. Aimon, H. K. Choi, X. Y. Sun, D. H. Kim, C. A. Ross, *Adv. Mater.*, 2014, **26**, 3063.
25. H. K. Choi, N. M. Aimon, D. H. Kim, X. Y. Sun, J. Gwyther, I. Manners, C. A. Ross, *ACS Nano*, 2014, **8**, 9248.
26. N. M. Aimon, D. H. Kim, H. K. Choi, C. A. Ross, *Appl. Phys. Lett.*, 2012, **100**, 092901.
27. Y.-H. Chu, Q. Zhan, L. W. Martin, M. P. Cruz, P.-L. Yang, G. W. Pabst, F. Zavaliche, S.-Y. Yang, J.-X. Zhang, L.-Q. Chen, D. G. Schlom, I.-N. Lin, T.-B. Wu, R. Ramesh, *Adv. Mater.*, 2006, **18**, 2307.
28. N. Dix, R. Muralidharan, J.-M. Rebled, S. Estradé, F. Peiró, M. Varela, J. Fontcuberta, F. Sánchez, *ACS Nano,* 2010, **8**, 4955.
29. T. Amrillah, S. K. Vandrangi, Y. Bitla, T. H. Do, S.-C. Liao, C.-Y. Tsai, Y.-Y. Chin, Y.-T. Liu, M.-L. Lin, Q. He, H.-J Lin, H.-Y Lee, C.-H. Lai, E. Arenholz, J.-Y. Juang, Y.-H. Chu, *Nanoscale*, 2016, **8**, 8847.
30. D. H. Kim, N. M. Aimon, C. A. Ross, *APL Mater.*, 2014, **2**, 081101.
31. L. Zhang, Y. Yuan, J. Lapano, M. Brahlek, S. Lei, B. Kabius, V. Gopalan, R. Engel-Herbert, *ACS Nano*, 2018, **12**, 1306.
32. L. Kornblum, J. Faucher, M. D. Morales-Acosta, M. L. Lee, C. H. Ahn, F. J. Walker, *J. Appl. Phys.*, 2018, **123**, 025302.
33. R. Comes, H. Liu, M. Khokhlov, R. Kasica, J. Li, S. A. Wolf, *Nano Lett.*, 2012, **12**, 2367.
34. V. Georgieva, A. F. Voter, A. Bogaerts, *Cryst. Growth Des*., 2011, **11**, 2553.
35. J-P. Maria, S. Trolier-McKinstry, D. G. Schlom, *J. Appl. Phys.*, 1998, **83**, 4373.
36. S. Wolf, *Proc. IEEE,* 2010, **98**, 2155.

Figure Captions

Figure 1. (a) Top view SEM image and **(b)** theta-two theta XRD scan of BFO-CFO nanocomposite sputtered at 650 ˚C on single crystalline Nb:STO substrate. R, C, and S denotes R-BFO, CFO and Nb:STO substrates, respectively. **(c)** φ scan of the BFO-CFO film on Nb:STO substrate. The source and

detector were set to the desired 2θ angle to detect specific peaks from the films, then the sample was tilted ~ 45˚ to record reflections from planes oriented at 45˚ to the film plane to observe the Nb:STO (202), BFO (202), and CFO (404). **(d)** X-ray diffraction reciprocal space maps of BFO-CFO for the asymmetric (103) reflection of BFO and Nb:STO substrate and the (206) reflection of CFO. The vertical and horizontal directions correspond to in-plane and out-of-plane, respectively. Inset is a schematic illustration of the epitaxial growth of BFO on Nb:STO substrate.

Figure 2. (a) Low magnified cross sectional TEM image of BFO-CFO nanocomposite grown on Nb:STO substrate using sputtering at 650 ˚C in 50 mTorr of working pressure. The ratio of Ar : O_2 was 1:4. The TEM sample was cut along Nb:STO [110]. **(b)** Magnified cross sectional TEM image of a CFO pillar in a BFO matrix on Nb:STO substrate. **(c)** High resolution TEM image of BFO-CFO interface and the fast Fourier transform (FFT) of selected BFO, CFO and whole area. **(d)** Cross-sectional low magnification TEM Z-contrast images of sputter grown BFO-CFO nanocomposite and elemental mapping of Bi, Fe, Co, Sr, and Ti.

Figure 3. (a) In-plane and out-of-plane hysteresis loops of sputter grown BFO-CFO nanocomposite thin films deposited at 650 °C. Inset is a magnified in-plane hysteresis loop. **(b)** Amplitude-voltage butterfly loop and phase-voltage hysteresis loop of BFO-CFO nanocomposite thin film. Simultaneous measurement of **(c)** topography and **(d)** amplitude images at the same area using PFM.

Figure 4. (a) Top view SEM image **(b)** XRD pattern of BFO–CFO nanocomposite grown on Nb:STO substrate at 650 ˚C in 50 mTorr with Ar:O_2 ratio of 1:9. T denotes T-BFO. **(c)** Room temperature VSM magnetic hysteresis loops of BFO-CFO nanocomposite grown at high oxygen ratio. Inset is a magnified in-plane hysteresis loop. **(d)** Amplitude and phase of BFO-CFO nanocomposite measured by PFM as a function of DC bias voltage.

Figure 5. (a) Top view and **(b)** 45˚ tilted SEM image of the BFO–CFO nanocomposite after etching in dilute HCl solution for 1 min at room temperature. The SEM image of the unetched sample corresponds to the sample in Fig. 5 (a). **(c)** Top view SEM image of BFO-CFO nanocomposite after etching for 3 min. **(d)** Magnified XRD patterns of BFO-CFO nanocomposites around the (001), (002) and (003) substrate peaks before and after etching for 1 and 3 min. A relaxed CFO peak which overlapped with the strained (002) R-BFO was clearly seen at 43.1˚ after removing the BFO. (**e,f**) Magnetic hysteresis loops of BFO-CFO nanocomposite after etching to remove BFO for **(e)** 1 and **(f)** 3 min.

Figure 6. (a) Top view SEM image **(b)** XRD pattern **(c)** Magnetic hysteresis loops of BFO–CFO nanocomposite grown on STO buffered Si substrate at 650 ˚C in 50 mTorr with Ar:O_2 ratio of 1:4. Inset is a magnified in-plane hysteresis loop. **(d)** Schematics of the templating procedure to make a periodic array of CFO nanopillars in a BFO matrix using FIB to pattern the Nb:STO substrate. (d)-1 Bombardment of Nb:STO substrate by an ion beam, (d)-2 Formation of nucleation cites by chemical etching, (d)-3 Growth of CFO seed in template using PLD, (d)-4 Growth of the ordered nanopillars by sputter deposition from a composite target **(e)** Top view SEM image of CFO nuclei in the template after etching and heat treatment. **(f)** Top view SEM image of the templated BFO-CFO nanocomposite.

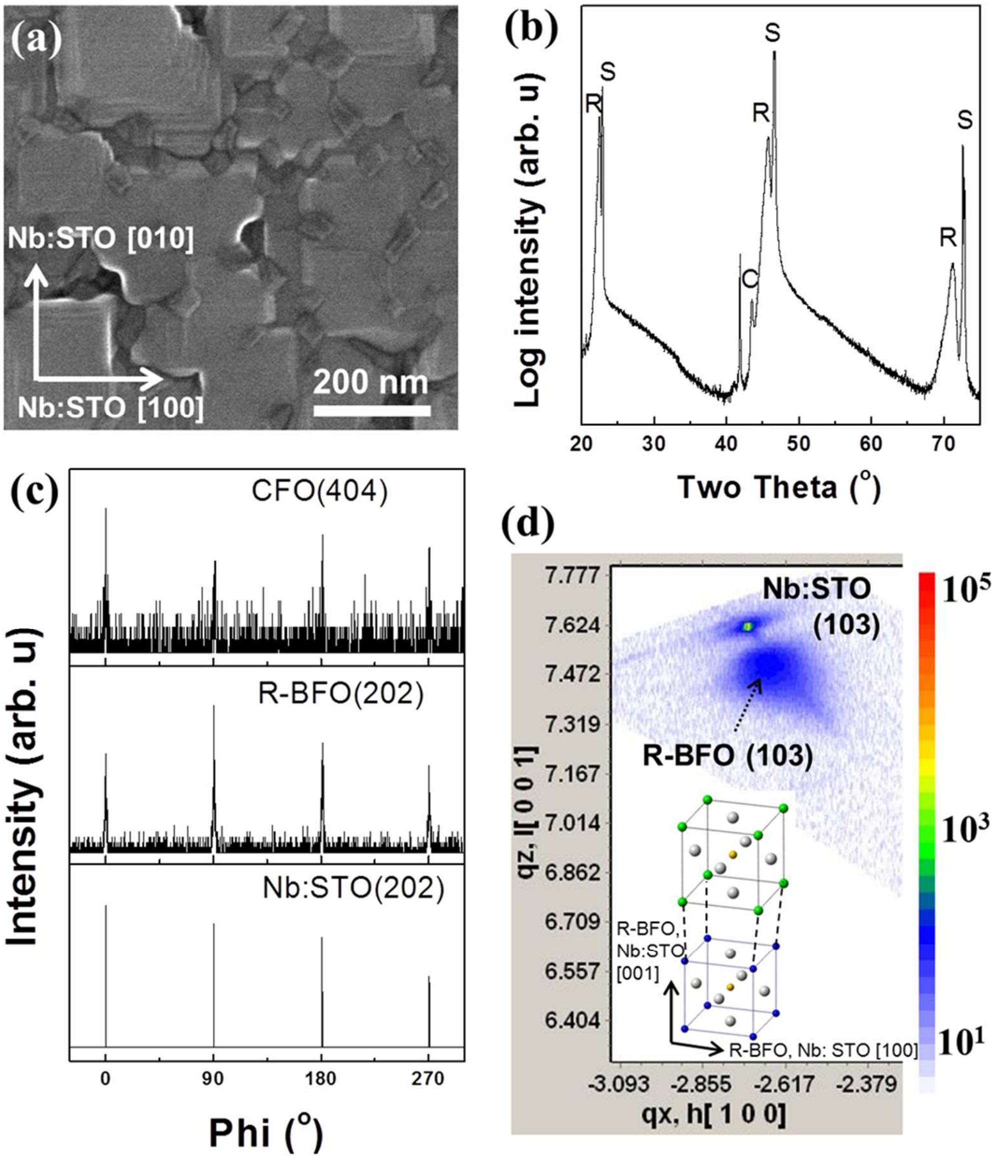

Figure 1

176x207mm (150 x 150 DPI)

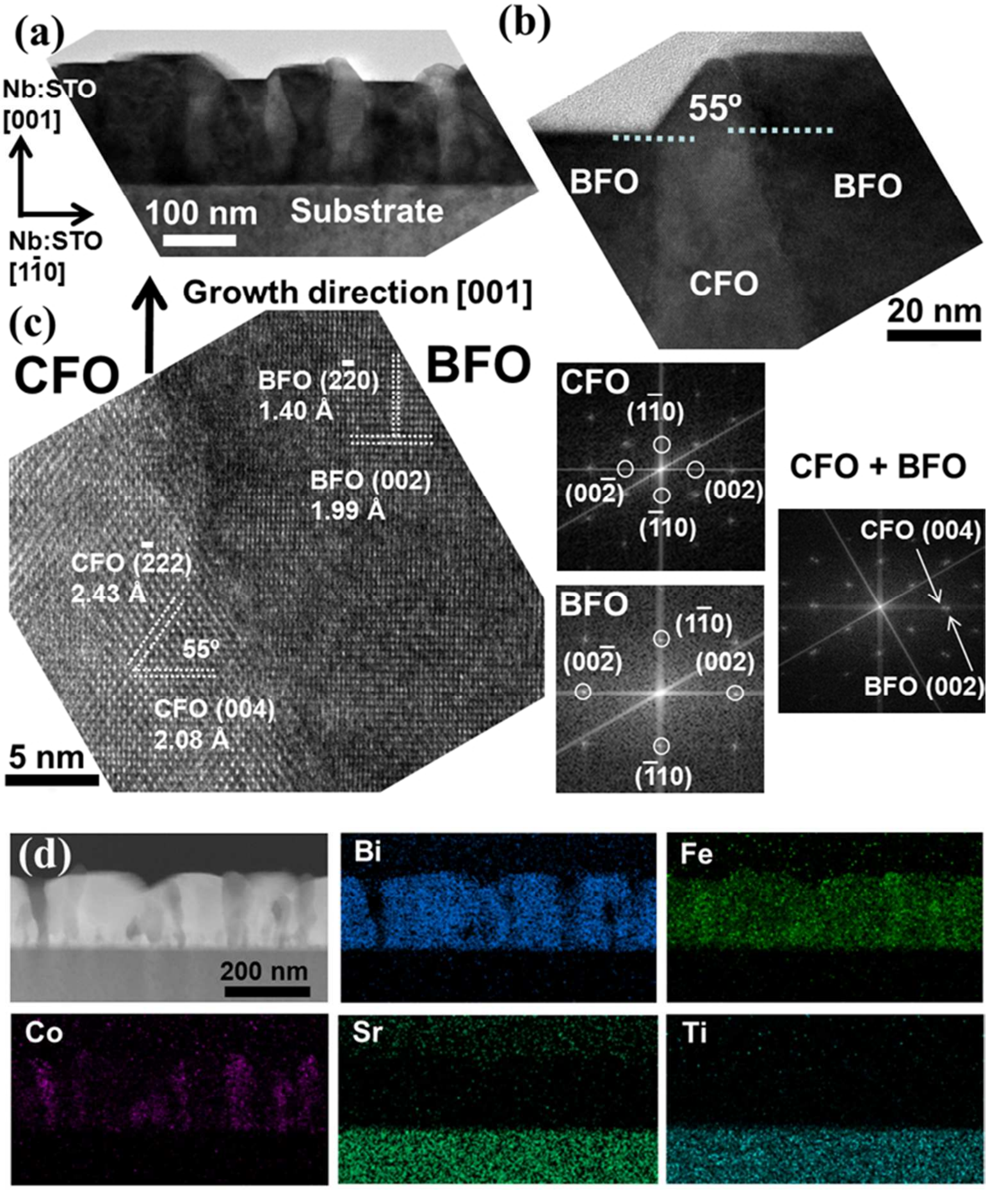

Figure 2

137x167mm (150 x 150 DPI)

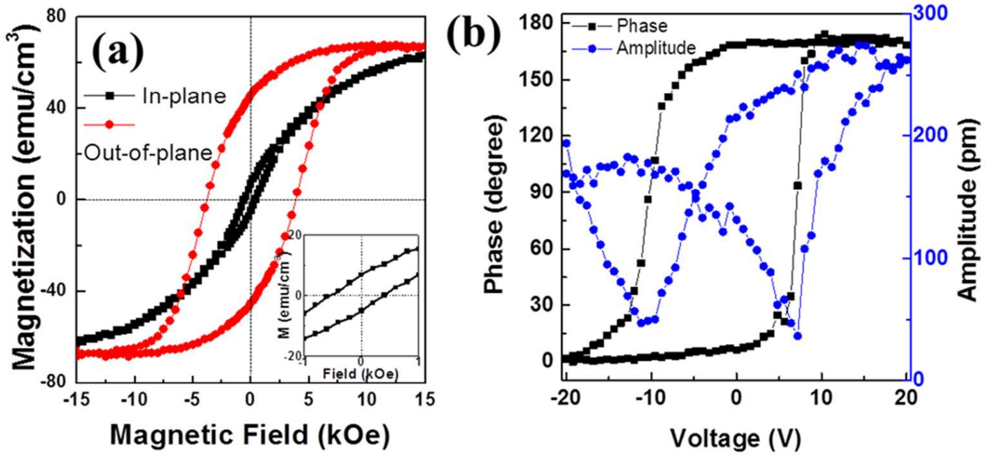

(c) PFM topography

(d) PFM amplitude

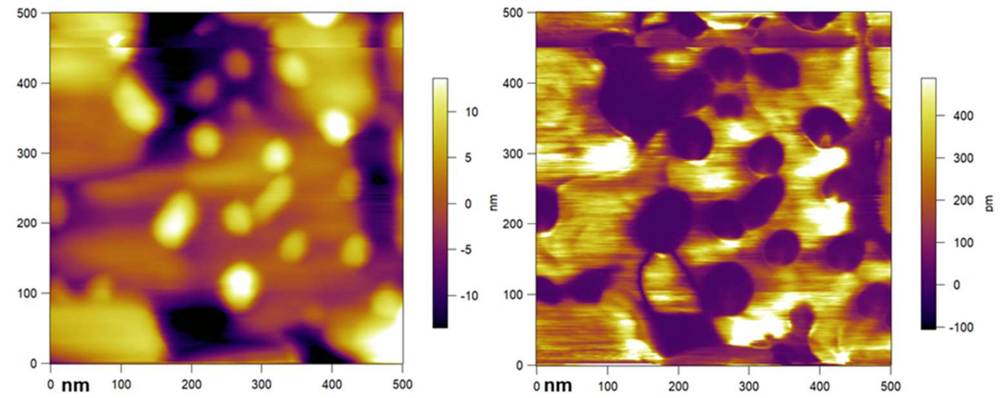

Figure 3

172x166mm (150 x 150 DPI)

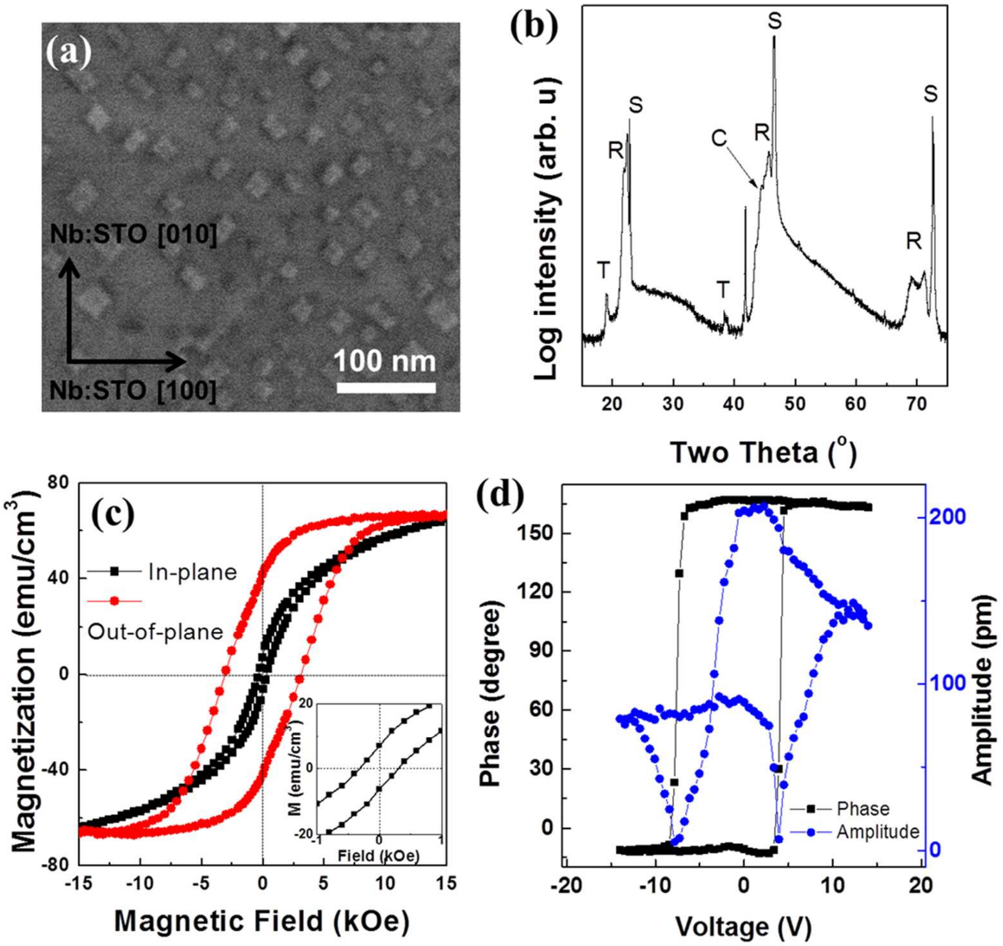

Figure 4

183x173mm (150 x 150 DPI)

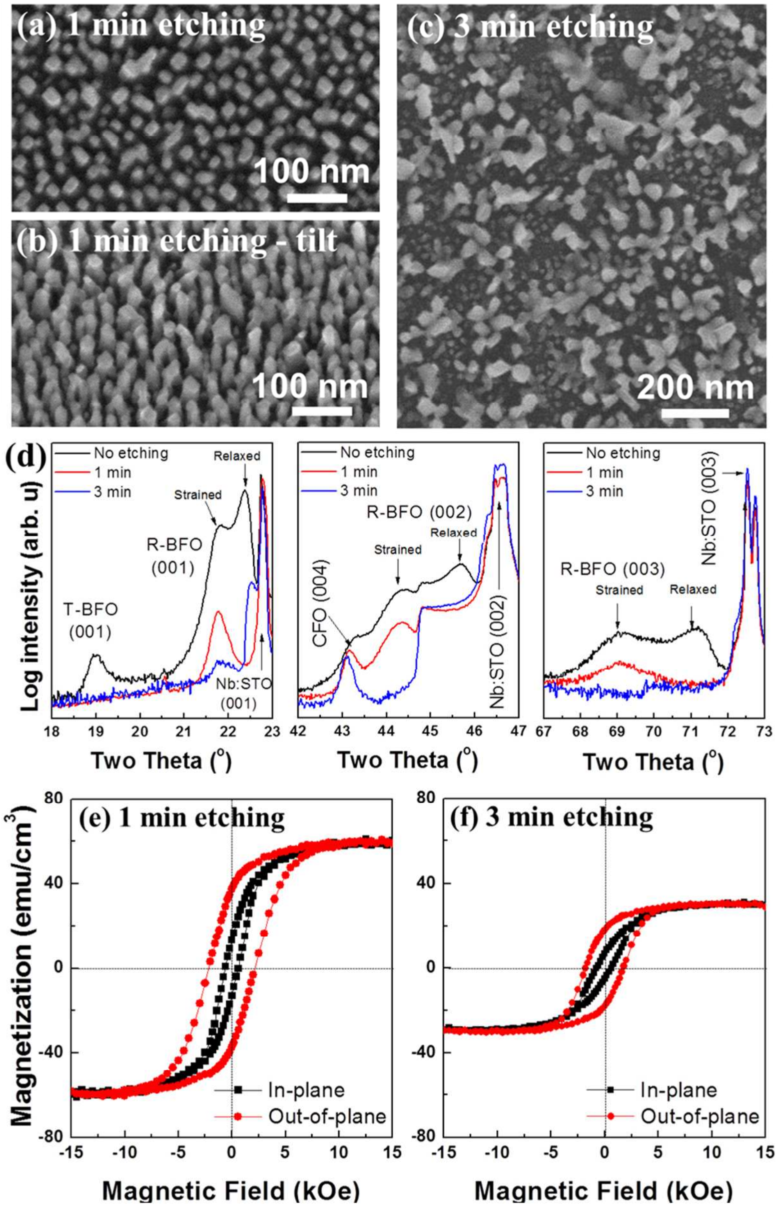

Figure 5

160x248mm (150 x 150 DPI)

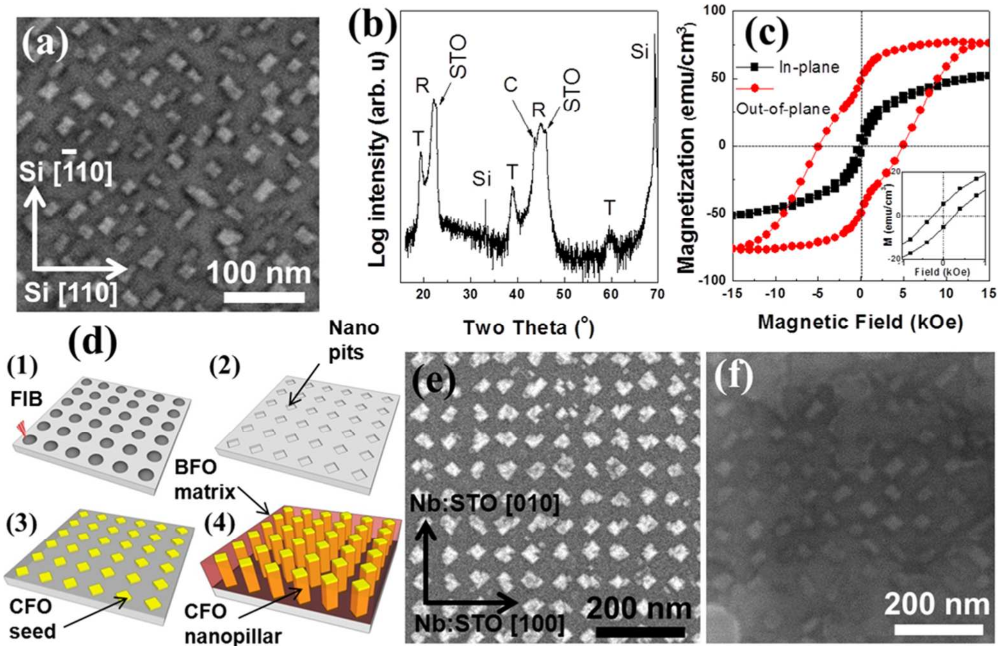

Figure 6

181x116mm (150 x 150 DPI)

A table of contents entry

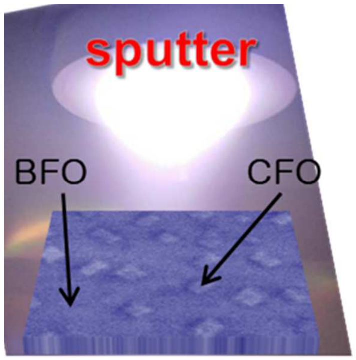

Sputter-grown self-assembled epitaxial spinel-perovskite nanocomposites consisting of $CoFe_2O_4$ pillars in a $BiFeO_3$ matrix on Nb-doped $SrTiO_3$ or $SrTiO_3$–buffered Si substrates